Research article

Supramolecular interaction between berberine hydrochloride and baicalin in aqueous solution: Reaction kinetics, spectral analysis and dynamic simulation

Hua Yang [a,1], Jiao Wang [a,b,1], Qiuru Tan [a], Zhi Dong [a], Zhizhong Yang [a], Peng Zhang [c,**], Wenping Wang [a,b,*]

[a] *College of Chinese Materia Medica, Yunnan University of Chinese Medicine, Kunming, Yunnan 650500, China*
[b] *Yunnan Key Laboratory of Southern Medicine Utilization, Yunnan University of Chinese Medicine, Kunming, 650500, China*
[c] *General Hospital of Ningxia Medical University, Yinchuan, Ningxia 750004, China*

A B S T R A C T

The current study presents a comprehensive investigation on the precipitation reaction and supramolecular interactions between berberine hydrochloride (BBR) and baicalin (BA) in an aqueous system. Utilizing a combination of multi-spectral analytical techniques and molecular dynamic simulations, we elucidated the mechanism of the complexion process. The precipitate formation was observed within a drug concentration range of 0.1–1.0 mM, and a 1:1 stoichiometry ratio of BBR to BA was established by the Job's plot method. Morphological and structural characterizations of the precipitates were conducted using DSC, FTIR and PXRD. Additionally, UV–Vis absorption and ^{1}H NMR spectroscopy were employed to compare the spectral characteristics of the precipitates with those of individual drug solution. Molecular dynamic simulations further dissected the intermolecular interactions and self-assembly mechanisms. The precipitates formed were amorphous microparticles with an average diameter of approximately 20 μm, primarily stabilized by hydrogen bonding and π–π stacking. This study contributes foundational insights into the supramolecular interactions between BBR and BA, therefore facilitated a better understanding of the precipitation process involving flavonoid-alkaloid pairs in mixed aqueous solutions.

1. Introduction

Berberine (BBR, Fig. 1A) and baicalin (BA, see Fig. 1B) are major active compounds extracted from Chinese medicinal plants of *Coptis chinensis* Franch (Huanglian, Chinese name) and *Scutellaria baicalensis* Georgi (Huangqin), respectively [1]. Huanglian and Huangqin are frequently used as a classic "medicine couple" in traditional complex prescriptions [2], including Gegen Qinlian decoction, Huanglian Jiedu decoction, Xiexin decoction and Shaoyao decoction. Notably, each of these prescriptions exhibits pronounced precipitation during the decoction process [3]. Similar precipitates were also observed in the decoctions of

---

* Corresponding author.
** Corresponding author.
E-mail addresses: zhp435656@163.com (P. Zhang), wangwenping@ynutcm.edu.cn (W. Wang).
[1] These authors contributed equally to this work as the co-first authors.
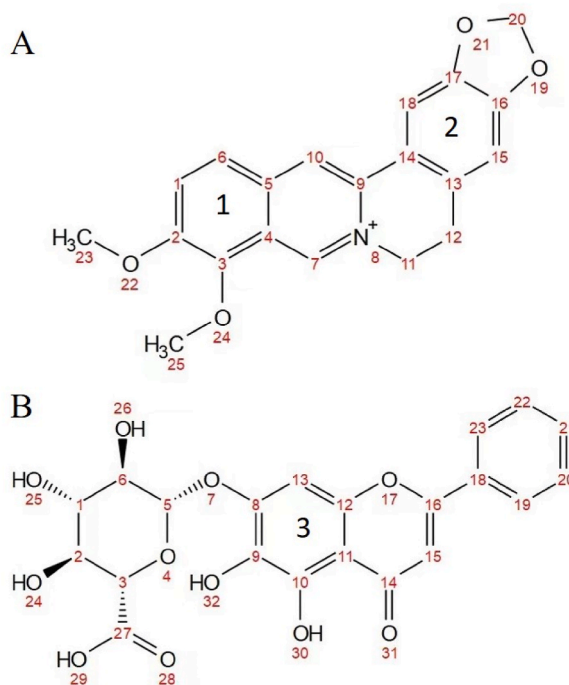
Fig. 1. Chemical structure of (A) Berberine and (B) Baicalin.

Huanglian-Huangqin pair [4] as well as in mixtures of BBR and BA solutions [5]. Consequently, there has been a surge in interest regarding the exploration of the potential therapeutic activities and applications.

The precipitates derived from the decoction or combined system of BBR and BA have demonstrated notable advantages in pharmacological efficacy and nano/microparticle architectures comparing to their parent compounds. Firstly, the BBR-BA complex was revealed a protective effect against neurotoxicity induced by cobalt chloride in differentiated PC12 cells [6]. Next, self-assembled BBR-BA nanoparticles were reported to display a robust affinity for bacterial cells, significantly enhancing their bacteriostatic activity. This enhancement led to the collapse of the disruption of bacterial populations and their biofilms [7]. Furthermore, these self-assembled nanoparticles, with an average diameter of 20 nm, when incorporated into a matrix of sodium carboxymethylcellulose and carrageenan, produced films that demonstrated photodynamic inactivation properties. These films were capable of harnessing sunlight to produce reactive oxygen species, effectively eliminating over 99 % of *Echerichia coli* and *Staphylococcus aureus* within 60 min [8]. However, it should be noted that the cocurrent administration of BBR may decrease the oral availability of BA by impeding flavonoid transport and modulating intestinal flora [9]. In light of these findings, the nanocrystals of BBR-BA complex have been developed using high-pressure homogenization to improve the dissolution rate and enhance the oral availability of both drugs [10].

Given the confirmed significance of the BBR-BA complex for pharmaceutical and therapeutical applications, elucidating the mechanism governing the precipitation process is essential for guiding future studies on analogous products. Yi et al. investigated the equilibrium concentrations between BBR and BA by HPLC analysis, and revealed the precipitate reaction as an exothermic process with a fixed molar ratio of 1:1 and a K_{sp} value of 1.01×10^9 mol^2/L^2 at 20 °C [11]. Wang et al. analyzed the binding heat and thermodynamic parameters of BBR-BA reaction using isothermal titration calorimetry method [12]. Their findings indicated a spontaneous and enthalpy-driven chemical reaction at a stoichiometric ratio of 1.002, with a Gibbs free energy (ΔG) of −35.573 kJ/mol and an association constant (K_a) of 1.228 1/M. Despite these insights, a comprehensive understanding of the supramolecular interactions between BBR and BA remains elusive.

To address this, our study delves into the reaction kinetics and characterization of the precipitation products of BBR and BA through a synergistic approach combing experimental techniques with coputational methods. This includes the application of multi-spectral analysis and molecular dynamic (MD) simulations to gain a deeper understanding of the complex interplay between these two bioactive phytochemicals.

2. Materials and methods

2.1. Materials

Berberine hydrochloride and baicalin (purity > 98 %) were supplied by Jingzhu Biotech Co., Ltd (Nanjing, China). Potassium bromide (KBr) for infrared spectroscopy was purchased from Guangfu Technology Development Co., Ltd (Tianjin, China). Various deuterated solvents were obtained from Cambridge Isotope Laboratories, Inc. Methanol and acetonitrile were of HPLC grade and other

chemicals were of analytical grade. All other reagents were used as received without further purification. All solutions in this study were prepared using purified or ultra-purified water provided by Arium® Comfort II system (Sartorius, Germany).

2.2. Reaction kinetics of BBR and BA

2.2.1. Precipitation observation on mixtures of BBR and BA

The solution of BBR or BA was prepared by dispersing and dissolving the bulk powder into purified water, respectively. And the pH of BA solution was adjusted to 8.0. Each drug solution was independently heated to 80 °C before mixing at a sequence of predetermined molar ratios. The obtained mixtures were then inspected on their appearance and laser scattering phenomenon at predetermined time intervals to ascertain the occurrence of precipitation.

2.2.2. Stoichiometry in complexation of BBR and BA

The Job's plot method was adopted to investigate the stoichiometry of BBR-BA complex [13]. Briefly, a set of solutions were prepared with equimolar BBR and BA at various volume fractions. The absorbance spectra of these solutions were recorded over a wavelength range of 200–600 nm using a T6 ultraviolet–visible (UV–Vis) spectrophotometer (Persee, China). A Job's plot was then constructed by plotting A_{268nm} against R, wherein $R = n\ BBR/(n\ BBR + n\ BA)$.

2.3. Preparation of BBR-BA complex

Pure BBR powder was precisely weighed and dissolved in purified water to prepare a 0.5 mM solution. BA solution of equivalent concentration was prepared in a dilute sodium hydroxide solution (pH = 8.0). These solutions were individually heated for 10 min at 80 °C followed by mixing in a 1:1 vol ratio. The mixture was allowed to cool to room temperature naturally before storage at 4 °C in a refrigerator overnight. After cooling, the mixture was then centrifuged at 10 000 rpm for 10 min to remove the supernatant. The precipitate was washed with water twice and then freeze-dried for 48 h. The resulting powder was collected and sealed before further investigation.

2.4. Morphology observation

The suspension of BBR-BA complex was dropped onto a slide and observed under an CKX53 invert microscope (Olympus, China). One drop of the suspension was spread onto a holder and air-dried at room temperature before undergoing 12 h of vacuum drying. A small amount of powder samples of pure drugs or their complex were mounted on a holder. The dry samples were then sputter-coated with a thin layer of gold for microstructural observation under a Phenom Pro scanning electronic microscope (SEM, Phenom-world BV, Netherlands).

2.5. Solid characterization of BBR-BA complex

2.5.1. Thermal analysis

Thermal properties of the samples were assessed using a Setsys16 differential scanning calorimeter (DSC, Setaram, France). Approximately 5 mg of powder samples were sealed in a aluminum pan and then heated from 30 °C to 350 °C at a rate of 10 °C/min under a nitrogen atmosphere.

2.5.2. Powder X-ray diffraction analysis

Powder X-ray diffraction (PXRD) patterns were recorded on a D8 Advance X-ray diffractometer (Bruker, Germany) with Cu-Kα radiation. The tube voltage and current intensity were of 40 kV and 30 mA, respectively. And data were collected over a 2θ range of 5° to 50° at a rate of 8°/min with a step size of 0.02°.

2.5.3. Fourier-transform infrared spectroscopy

The functional group interactions within the BBR-BA complex were analyzed by Fourier-transform infrared (FTIR) spectroscopy. The samples were thoroughly mixed with KBr in an agate mortar and subsequently pressed into thin disks by a hydraulic press. FTIR spectra were then collected by a Great20 FTIR spectrophotometer (Zhongke Ruijie, China) with the following parameters: scanning range of 4000 to 400 cm^{-1}; wavenumber resolution of 2 cm^{-1}; transmission percentage mode; 64 cumulative scans at room temperature.

2.6. Liquid characterization of BBR and/or BA solutions

2.6.1. UV–vis spectroscopy

The pure drugs or their complex were dissolved in methanol to give a clear solution. Then the absorption spectra of these solutions were recorded using the UV–Vis spectrophotometer. Quartz cuvettes with a 10 mm path length were filled with 2 mL of solutions. All samples were scanned in a range of 200–600 nm at a fixed slit width of data interval of 1 nm.

2.6.2. Nuclear magnetic resonance hydrogen spectrometry (^1H NMR) analysis

Powders of pure drugs (10 mg) or their complex (15 mg) were weighed and dispersed into 1 mL deuterium dimethyl sulfoxide (DMSO-d_6). The resulted solutions were then scanned 16 times by a Bruker Advance 400 MHz NMR apparatus (Bruker, Germany) with tetramethylsilane (TMS) as an internal standard.

To further analysis the complexion formation mechanism, individual BA and BBR solutions were prepared in DMSO-d_6, mixed in a 1:1 M ratio, and diluted with deuterium hydrogen oxide (D$_2$O). The obtained mixtures at a range of concentrations were then scanned 256 times to collect their ^{1}H NMR spectra [14]. Next, the mixture at 500 mM were added with different additives (10 %, w/v) to further investigate the intermolecular interactions via ^{1}H NMR analysis [15].

2.7. Molecular dynamic simulation

Molecular dynamic (MD) simulations were conducted using Gromacs 2022.6 program [16]. The conformation of BBR and BA were initially optimized at a B3LYP-D3(BJ)/def2-TZVP level, followed by single-point energy calculations using ORCA 5.0.3 software [17]. RESP2 charge fitting [18] was carried out with Multiwfn [19], and the general AMBER force field (GAFF) parameters were generated by Sobtop software [20]. An opc3 water model box containing 25 molecules each of BBR and BA was prepared and neutralized by Cl$^-$. The system underwent energy minimization by the conjugate gradient method. The system was pre-equilibrated for 200 ps (ps) in the NPT ensemble. And the MD simulation was then performed at 298.15 K and 1 atm using the v-rescale temperature and Parrinello-Rahman pressure coupling methods. Particle mesh Ewald (PME) method was applied to calculate the electrostatic interactions with a cutoff distance of 1 nm. Production simulations were performed for 100 ns (ns), with a trajectory frame interval set at 5 ps.

The potential interactions within BBR-BA, BBR-BBR or BA-BA dimers were analyzed using Molclus 1.9 [21] software and visualized with Multiwfn and VMD [21]. Dimers conformations were generated using Genmer with a "rmax" value of 6, and 10 conformations with the lowest energy were retained after preliminary optimization with PM6-D3 level via MOPAC software. Vibrational analysis was conducted using a B3LYP-D3(BJ)/6-31+G (d, p) method, and 5 confirmations with the lowest energy were selected for single-point energy calculation with ORCA, employing a B3LYP-D3(BJ)/def2-TZVP functional and basis set along with a SMD solvent model. The obtained values were combined with calibrated free energy to determine the final free energies. The conformation with the lowest free energy was depicted using the independent gradient model based on Hirshfeld partition (IGMH) [22]. Furthermore, the inter-molecular interaction energies for each dimer pair were calculated using the sobEDAw method [23] as follows:

$$\Delta E_{int} = \Delta E_{els} + \Delta E_{xrep} + \Delta E_{orb} + \Delta E_{disp}$$

In which the total interaction energy (ΔE_{int}) was decomposed to be electrostatics term (ΔE_{els}), the exchange-repulsion term (ΔE_{xrep}), the orbital interaction term (ΔE_{orb}) and the dispersion term (ΔE_{disp}). All these terms were calculated by ORCA with a B3LYP-D3(BJ)/6-311+G (2d, p) functional and basis set.

3. Results and discussion

3.1. Precipitation phenomenon of BBR-BA mixtures

The images for mixtures of BBR and BA at various ratio and different timepoints were provided in the supplementary file (see Fig. S1–S3). All mixtures were categorized into two groups based on the occurrence of precipitation or not: the "−" group showed a clear appearance without obvious laser pathway, while the "+" group could be observed with suspending particles and/or obvious laser pathway. The "+" samples were then plotted according to BBR:BA molar ratio and storage period of the mixtures. The resulted
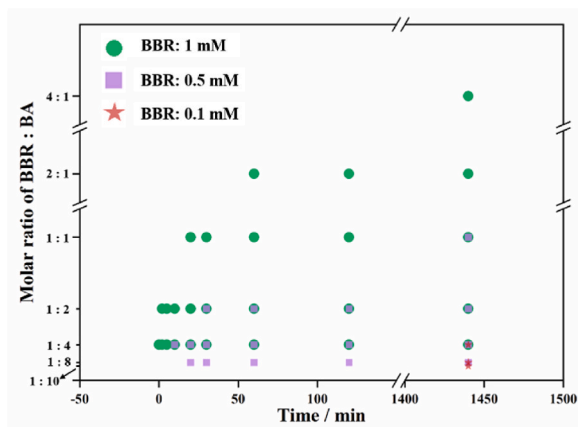

Fig. 2. Phase diagram for precipitated mixtures of BBR and BA.

phase diagram for precipitation was depicted in Fig. 2.

Obviously, the higher values of drug concentration or molar ratio of BBR to BA, the quicker formation and larger quantity of precipitates in the mixed system of BBR and BA. And in appearance, the particle size of the resulted precipitates gradually increased over time.

3.2. Stoichiometry in BBR-BA complexation process

Fig. 3A presents the absorption spectra of 0.042 mM BBR with increasing concentrations of BA. The maximum absorption wavelength (λ_{max}) of BBR in water was identified as 268 nm (benzene ring) and 330 nm (C]N$^+$). Upon the addition of BA, the spectra showed a discernible shift in the absorbance peaks, which is indicative of complexation interactions. Specifically, a red shift is observed from 263 nm to 268 nm, and a blue shift is noted from 342 to 335 nm. The red shift suggested the formation of an ion-pair complex between BBR and BA, which was stabilized by electrostatic binding, π-π stacking, hydrogen bonding, and hydrophobic interactions [24]. This interpretation is consistent with the J-type aggregation model, which posit an anti-parallel (head-to-tail) arrangement of BBR molecules [25]. It is important to note that while the intensity of BBR gradually increased with the addition of BA, the wavelength of maximum intensity does not shift significantly, indicating that the BBR-BA complex likely forms through ion-pair formation and subsequent precipitation in the aqueous solution.

Using the Job's method, the complexation ratio of BBR and BA was evaluated, as depicted in Fig. 3B. The Job's plot clearly shows a maximal value of A $_{268nm}$ at an R value of approximately 0.5, confirming a 1:1 stoichiometry for the BBR-BA complex. This finding suggested that BBR and BA contributed equally to the formation of the ion-pair complex.

3.3. Morphology observation

As shown in Fig. 4A, BBR or BA solution was clear and transparent without obvious Tyndall effect, which is indicative of the absence of suspended particles. However, upon mixing, the resulting suspension exhibited a pronounced Tyndall effect due to the formation of suspended particles that scattered laser light. Numerous bright yellow granules were observed within the suspension of BBR-BA mixture (Fig. 4B). These granules appeared as regular particles, approximately 20 μm in diameter, often connected in lines or clusters. Further observation under TEM (Fig. 4C) resolved these granules into aggregates of spherical nanoparticles, each about 20 nm in size, which was consistent with previous report [8]. SEM observation (Fig. 4D) distinguished the raw BBR as regular prisms with width of around 3 μm and varying lengths, while BA appeared as aggregates of small, flaky particles. The BBR-BA complex, in contrast, manifested as irregularly shaped granules with a crimp texture and fine particles adhering to their surface.

Combining the morphological observations, it is evident that the micro-sized particles in BBR-BA mixture were aggregates of nano-sized entities. The presence of microparticles in this study, as opposed to the nanoparticles reported previously [3], could be attributed to the significant higher drug concentrations in the mixed system. Additionally, it is suggested that the observed microparticles might underwent a morphological transformation, collapsing in shape during the drying process. These finding s underscore the influence of dug concentration and processing conditions on the resulting physical form of the BBR-BA complex.

3.4. Solid characterization

3.4.1. Thermal analysis

To elucidate the thermal properties of BBR-BA complex, DSC and thermogravimetry (TG) analyses was carried out, with the results presented in Fig. 5.

As shown in Fig. 5A, BBR exhibited two endothermic peaks at 100 °C (water loss) and 145 °C (melting), and an exothermic peak at 200 °C (degradation), which is in consistence with other studies [8]. BA displayed two endothermic peaks at 220 °C (melting) and
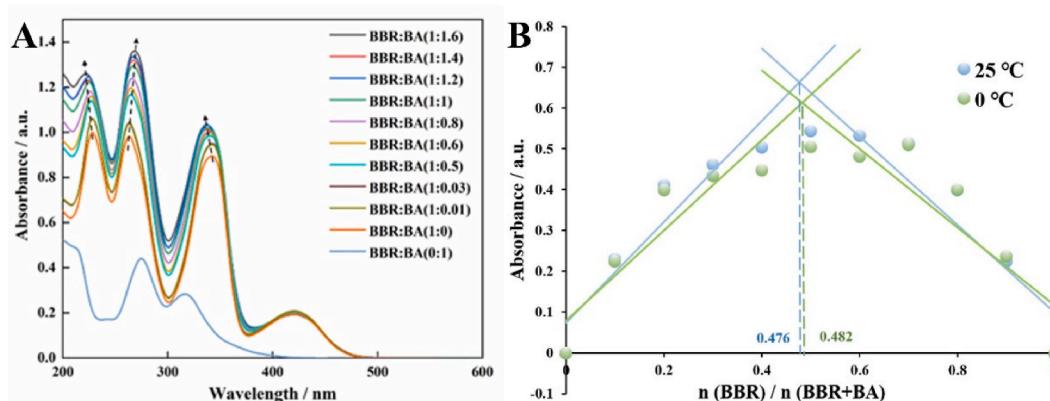

Fig. 3. (A) Equimolar continuous variation curve and (B) Job's plot of the BBR-BA complex at 25 °C and 0 °C.
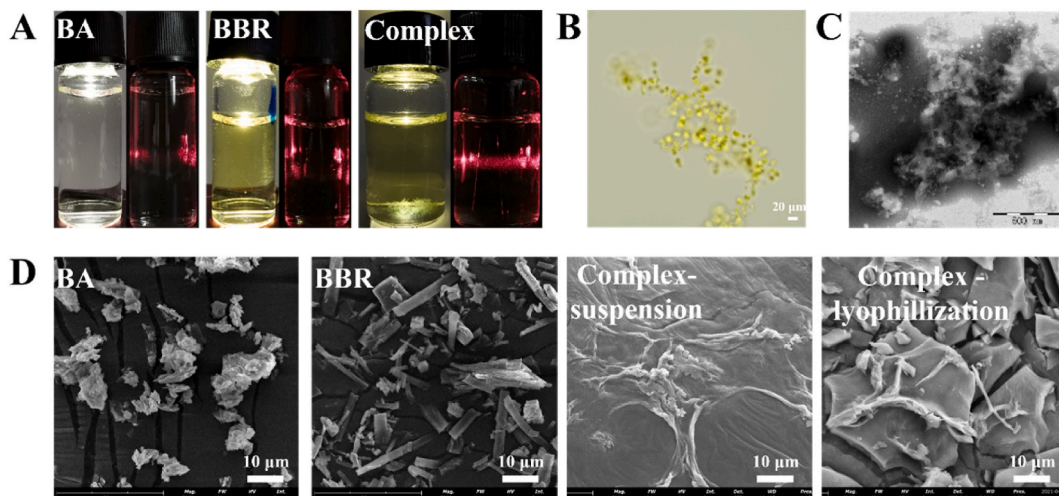
Fig. 4. (A) Appearance drug solutions and their complex system, and micromorphological images of BBR-BA precipitates under (B) optical microscopy, (C) TEM or (D) SEM.
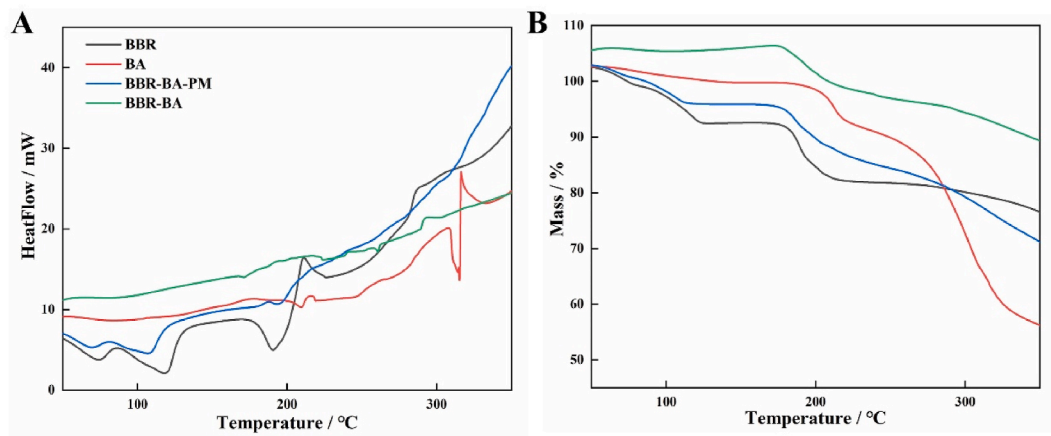

Fig. 5. (**A**) DSC and (**B**) TG curves of pure BBR, BA, their physical mixture and complex.
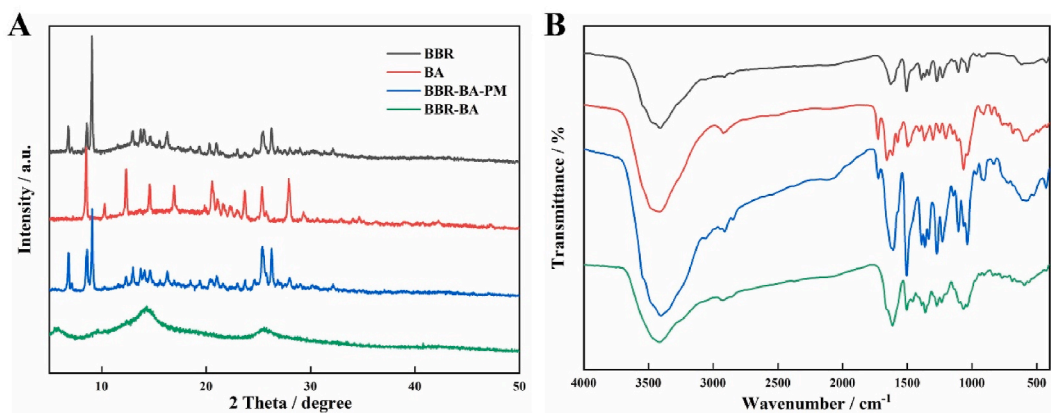

Fig. 6. (A) PXRD and (B) FTIR patterns of pure BBR, BA, their physical mixture and complex.

330 °C (degradation) [10]. The physical mixtures of two drugs (BBR-BA-PM) retained peaks similar to the original drugs, whereas the complex showed no obvious peaks, suggesting interactions had occurred during the co-precipitation process. The TG curves in Fig. 5B further support these observations. The maximum rate of mass loss for the BBR-BA complex was significantly lower compared to the pure drugs and their physical mixture, indicating a reduced degradation rate and enhanced thermal stability for the complex [8]. These thermal analyses provide valuable insights into the stability and integrity of the BBR-BA complex, which are crucial for its potential pharmaceutical applications and storage considerations.

3.4.2. Powder X-ray diffraction

In PXRD analysis, both BBR and BA showed crystalline forms with intense diffraction peaks in the 3–35° 2θ range (Fig. 6A), consistent with prior studies [10]. Multiple diffraction peaks at 2θ of 6°, 8°,9°, 25° and 26° indicated the presence of BBR in BBR-BA-PM. The peaks at 2θ of 8°,12°, 25° and 28° with reduced intensity could be assigned to BA in BBR-BA-PM. However, the BBR-BA complex displayed only a few broad peaks in its diffractogram, suggesting an amorphous state of the precipitates formed during the co-assembly process of BBR and BA in aqueous media.

Li et al., who prepared BBR-BA nanoparticles using a similar method, reported a crystalline form that more closely resembled pure BBR [7]. Their nanoparticle diffraction pattern was analogous to the physical mixture observed in this study. The discrepancy in the crystallinity of the products may be attributed to variations in the sample preparation processes and the size of the particles obtained.

3.4.3. Frontier-transform infrared spectroscopy

FTIR spectroscopy was applied to analyze any molecular interaction between BBR and BA of complex in the powdered state. The spectra of pure BBR, BA, their physical mixture and complex were depicted in Fig. 6B. The main characteristic vibrational modes of drug molecule can be assigned as follows: O–H stretching at ~3400 cm^{-1} for BBR and BA; C]C vibrations at 1505 cm^{-1} for BBR; C–O–C vibrations at 1076 cm^{-1} for BA. The spectra of complex showed characteristic peaks of both BBR and BA with some difference: a blue shift from 1720 cm^{-1} (carboxyl group) to 1656 cm^{-1} (carboxyl group); a blue shift from 1632 cm^{-1} (C]N$^+$) to 1620 cm^{-1} (amide II band). These spectral changes suggest the presence of electrostatic interaction between carboxyl group of BA and the C–N group of BBR during the complex formation [3]. These findings provide evidence of the molecular interactions that contribute to the formation and stability of the BBR-BA complex.

3.5. Liquid characterization

3.5.1. Ultraviolet–visible spectroscopy

Fig. 7A displays the UV–vis absorbance spectra of the pure BBR and BA, and their complex in methanol solution at predetermined concentrations. BBR's spectra were characterized by four distinct absorption peaks: 231 nm (homoannular diene), 266 nm (benzene ring), 350 nm and 429 nm (the conjugated system of isoquinoline rings). BA's spectra revealed three peaks: 216 nm (conjugated double bond) and 278 nm (benzene ring). Notably, the BBR -BA complex showed four characteristic absorption peaks at 217 nm, 272 nm, 350 nm and 430 nm, suggesting complex formation.

3.5.2. NMR spectra

To further investigate the types and positions of molecular interactions between BA and BBR, the ^{1}H NMR spectrum of the complex was collected and compared with those of the individual drugs. The assignments and the chemical shifts of the H signals were detailed in Tables S1 and S2 of the supplementary file. Upon complexation (Fig. 7B), the H signals in BBR shifted up-field from 8.21, 8.00, 4.07 ppm to 8.12, 7.94, 3.99 ppm, respectively, while those in BA moved from 5.25, 4.07 ppm to 4.98, 3.61 ppm. Additionally, the H signals on BA's B ring showed a noticeable shift from down-field to up-field, indicating participation of the B ring of BA and the isoquinoline
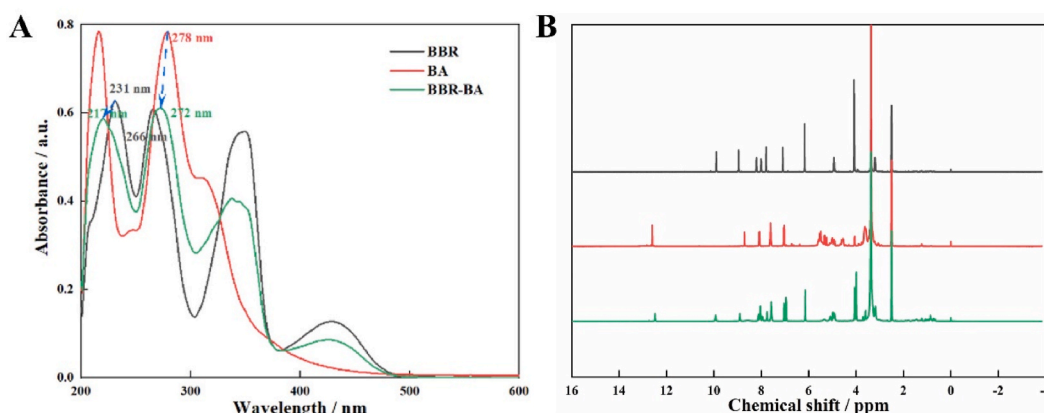

Fig. 7. (A) UV–vis and (B) ^{1}H NMR spectra of pure BBR, BA and complex in methanol.
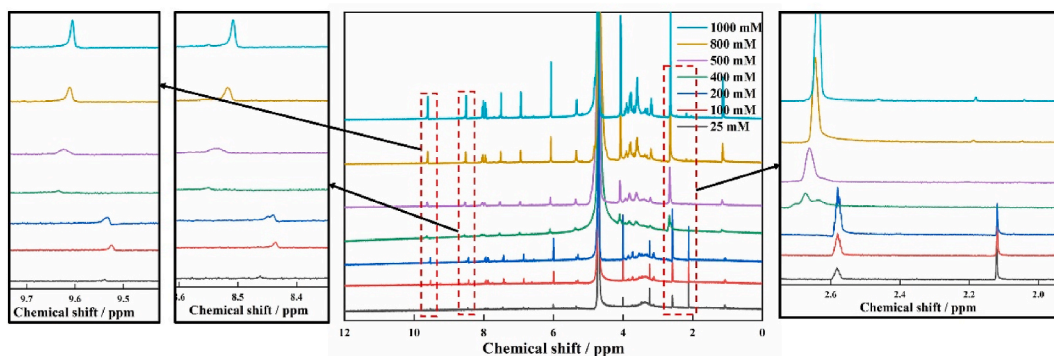
Fig. 8. ^{1}H NMR spectra of BA-BBR solutions.

ring of BBR in π-π stacking.

Fig. 8 shows the ^{1}H NMR spectra of BA-BBR solutions, where the intensity of resonance peaks intensified with increasing concentration. At higher concentrations, more resonances were observed, particularly in the 3–4 ppm range. The peak shapes evolve from sharp to broad, suggesting a transition from monomeric or oligomeric species to larger assemblies. Significant resonance shifts were revealed at concentrations of 400 mM and above, particularly for H-7, H-10 and 23-OCH$_3$ of BBR. The appearance of suspending particles in these mixtures further supports this transition.

Fig. 9 illustrates the ^{1}H NMR spectra of BA-BBR solutions with various additives. The spectra reveal changes in the intensity, shift and number of resonance peaks, with the peak for 23-OCH$_3$ of BBR around 2.6 ppm showing a significantly up-field shift and sharpening. Similar shifts were observed for peaks in the 6–10 ppm range. Among the additives, SDS caused the most distinct changes in the NMR spectra and results in substantial precipitate formation, indicating its significant disruption of BA-BBR complex. According to previous reports [14], glucose or urea can disrupt intermolecular hydrogen bonding, betaine and NaCl can inhibit electrostatic interactions, and SDS can disrupt the hydrophobic interactions during self-assembly, while NaCl can have an opposing effect.

The ^{1}H NMR analysis thus confirmed that hydrogen bonding, electrostatic and hydrophobic interactions all attributed to the co-assembly process of BA and BBR, providing a deeper understanding of the molecular interactions that drive the formation and behavior of their complex in aqueous solutions.

3.6. Molecular dynamic simulation

MD simulations provided insights into the complexation dynamics of BBR and BA. As shown in Fig. 10, 25 molecules each of BBA and BA were initially dispersed randomly into the water box. Within the first 30 ns, hydrophobic interactions led to the formation of a dozen aggregates, which further coalesced into larger structures by 100 ns. Within these aggregates, the polycyclic backbones of drug molecules engaged in π–π stacking, leading to the formation of a tightly interconnected network.

The key simulation parameters were depicted in Fig. 11. The RMSD value of the system (Fig. 11A) rapidly increased to approximately 5.5 nm within the initial 5 ns and then fluctuated around this value. The solvent accessible surface area decreased from about 270 nm^2 to 130 nm^2 over the 100 ns simulation (Fig. 11B). The number of hydrogen bonds between BA-BA molecules slowly increased from 25 up to 35 (Fig. 11C), while no significant hydrogen bonding was observed between BBR-BA molecules throughout the simulation.

Coul-SR represented the electrostatic interactions and can be assumed to the contribution of hydrogen bonding, and LJ-SR
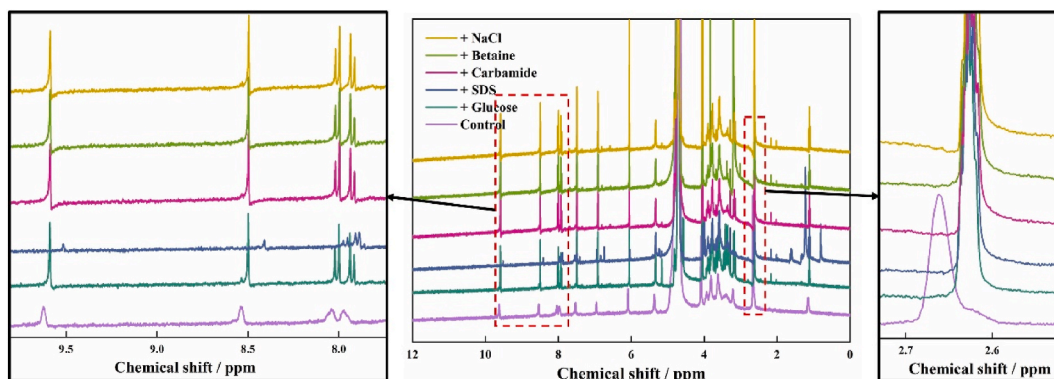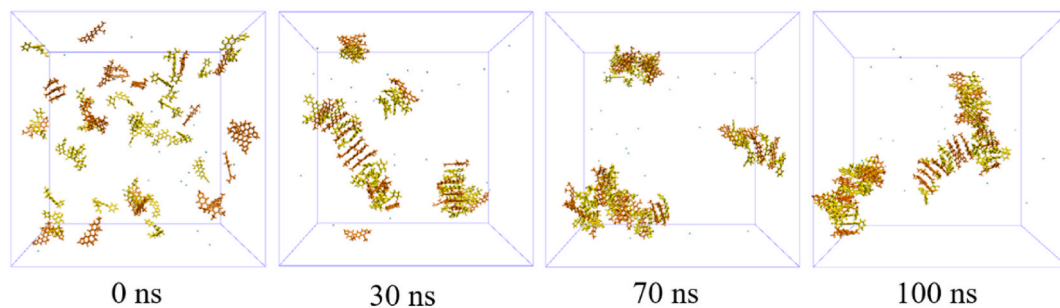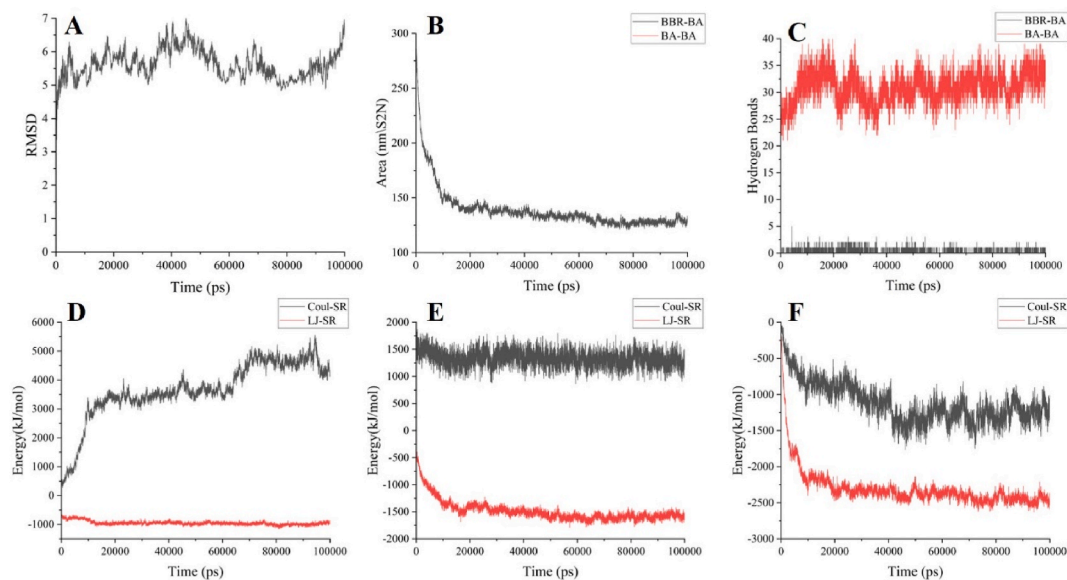

Fig. 9. ^{1}H NMR spectra of BA-BBR solutions.

**Fig. 10.** Snapshots for complexation of BBR and BA during the molecular dynamic simulation process.

Fig. 11. (A) RMSD value; (B) solvent accessible surface area, (C) number of drug-drug hydrogen bonds of the BBR-BA complex, and energy change of (D) BBR-BBR, (E) BA-BA and (F) BBR-BA systems during MD simulation process.

represented the Van Der Waals interaction primarily denoting π–π interactions [[21,26]]. As shown in Fig. 11D and E, the positive system energy values for BBR-BBR and BA-BA suggested strong electrostatic repulsion, with the former increasing significantly and the latter decreasing slightly during the simulation process. The Van Der Waals interactions for these two drug dimers exhibited a slight decline. In contrast, both electrostatic attraction and Van Der Waals interactions between BBR-BA molecules intensified throughout the simulation (Fig. 11F), suggesting that self-aggregation was predominantly driven by these forces. The main parameters of π–π stacking interactions between BBR and BA molecular aromatic rings are presented in Table S3 (see Supplementary File).

Fig. 12 presented IGMH maps that delineate the intermolecular interactions between drug molecules, as indicated by the color bar [22]. The extensive green isosurface for the BBR-BBR complex (Fig. 12A) highlighted a significant van del Waals interaction, likely due to the absence of hydrogen bond acceptors. A single hydrogen bonding was identified between BBR and BA (Fig. 12C), and the BA-BA (Fig. 12B) complex also displayed van del Waals and hydrogen bond interactions.

Table 1 summarizes the interaction energies of different dimers calculated using the sobEDAw method. The dispersion energy was found to be the most substantial contributor, exceeding both electrostatic and orbital interaction energies during dimer complexation. The total interaction energies for the three dimers decreased in the order of BA-BA, BBR-BA, and BBR-BBR. The negative ΔE_{int} values for the BA-BA and BA-BBR complexes indicated spontaneous complex formation, while the positive value for BBR-BBR suggested that dimer formation would not occur in the gas phase due to strong repulsion. However, the solvent environment in the MD simulation facilitated dimer formation despite the electrostatic repulsion.

Integrating the MD simulation results with the characterization data, it is now evident that the complexation between BBR and BA was primarily driven by intermolecular hydrogen bonding and π–π stacking, leading to precipitate formation in the aqueous solution system [27]. This comprehensive analysis enhances our understanding of the molecular interactions underlying the precipitation process and provides a foundation for further exploration of similar systems.
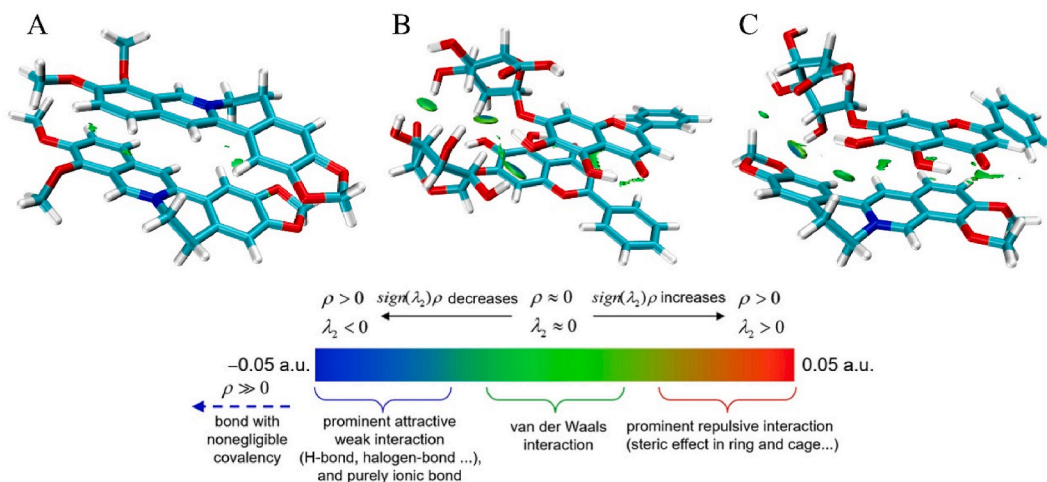
Fig. 12. IGMH maps for complexes of (A) BBR-BBR, (B) BA-BA and (C) BBR-BA. (The color bar at the bottom represented the value of *Sign* $(\lambda_2)\rho$ in the isosurface by filling colors, and the hydrogen bonds were marked by blue arrows.).

Table 1
The interaction energy of different dimers based on the sobEDAw method (Kcal/mol).

Type	ΔE_{int}	ΔE_{els}	ΔE_{xrep}	ΔE_{orb}	ΔE_{disp}
BBR-BBR	19.90	35.94	39.71	−8.15	−47.60
BA-BA	−36.86	−27.70	53.14	−17.16	−45.14
BBR-BA	−32.05	−25.98	48.50	−11.35	−43.22

4. Conclusions

The present study delves into the precipitation dynamics of self-aggregated BBR-BA complexes, pinpointing the concentration range of their formation through morphological observation. Using Job's method, we have confirmed a 1:1 stoichiometric ratio for the complexation of BBR and BA molecules in aqueous environment. The obtained dual-drug complex was characterized as uniform microspheres composed of nanoparticles in an amorphous state. FTIR, ^{1}H NMR and MD simulation analysis highlighted the pivotal roles of hydrogen bonding, electrostatic interactions and hydrophobic effects in the complexation process.

This investigation not only enhances our comprehension of the intricate supramolecular interactions between BBR and BA but also serves as a valuable reference for future explorations into the co-assembly reactions involving flavonoids with alkaloids. The insights gained from this study are instrumental in guiding the design and development of novel pharmaceutical formulations that leverage the synergistic properties of such bioactive drug pairs. However, the current research is limited by the *in vitro* nature of the experiments conducted, and further *in vivo* studies are needed to assess the pharmacokinetics and pharmacodynamics of the BBR-BA complex in animal models, as well as exploring its potential applications in novel drug delivery systems.

Data availability statement

Data will be made available on request.

CRediT authorship contribution statement

Hua Yang: Writing – original draft, Methodology, Formal analysis. **Jiao Wang:** Writing – original draft, Methodology. **Qiuru Tan:** Methodology, Formal analysis. **Zhi Dong:** Methodology, Formal analysis. **Zhizhong Yang:** Methodology, Formal analysis. **Peng Zhang:** Writing – review & editing, Funding acquisition, Formal analysis. **Wenping Wang:** Writing – review & editing, Funding acquisition, Conceptualization.

Declaration of competing interest

The authors declare that they have no known competing financial interests or personal relationships that could have appeared to influence the work reported in this paper.

Acknowledgments

The authors are grateful to National Natural Science Foundation of China (No. 82360778), and Applied Basic Research Joint Special Funds on Chinese Medicine of Yunnan Provincial Science and Technology Department (202301AZ070001-059) for their financial support. This study was also partly supported by Natural Science Foundation of Ningxia Hui Autonomous Region (2022AAC03578) and the Reserve Talents Project for Young and Middle-Aged Academic and Technical Leaders of Yunnan Province (grant no. 202205AC160038).

Appendix A. Supplementary data

Supplementary data to this article can be found online at https://doi.org/10.1016/j.heliyon.2024.e29992.

References

[1] L. Jiang, Y. Xiong, L. Yu, Y. Chen, Q. Zhang, X. Ding, X. Yan, P. Nie, G. Xu, Simultaneous determination of seven active components in rat plasma by UHPLC-MS/MS and application to a quantitative study after oral administration of Huang-Lian Jie-Du decoction in high Fat-induced atherosclerosis rats, Int. J. Anal. Chem. 2019 (2019) 5628160, https://doi.org/10.1155/2019/5628160.

[2] Han-Young Kim, Jung-Hoon Kim, Chemical influence of Scutellaria baicalensis—coptis chinensis pair on the extraction efficiencies of flavonoids and alkaloids at different extraction times and temperatures, Separations 10 (2) (2023) 131, https://doi.org/10.3390/separations10020131.

[3] M. Chen, P. Wang, T. Li, L. Li, J. Li, H. Bai, H. Lei, Q. Ma, Comprehensive analysis of Huanglian Jiedu decoction: revealing the presence of a self-assembled phytochemical complex in its naturally-occurring precipitate, J. Pharm. Biomed. Anal. 195 (2021) 113820, https://doi.org/10.1016/j.jpba.2020.113820.

[4] J. Wang, D. Zheng, N. Xu, et al., Attribution and identification of absorbed components by HPLC-DAD-ESI-MS after oral administration of Erhuang decoction, J. Anal. Sci. Technol. 11 (2020) 38, https://doi.org/10.1186/s40543-020-00236-4.

[5] J.R. Wang, T. Tanaka, H. Zhang, I. Kouno, Z.H. Jiang, Formation and conformation of baicalin-berberine and wogonoside-berberine complexes, Chem. Pharm. Bull. 60 (6) (2012) 706–711, https://doi.org/10.1248/cpb.60.706.

[6] C. Zhang, R. Zhao, W. Yan, H. Wang, M. Jia, N. Zhu, Y. Zhu, Y. Zhang, P. Wang, H. Lei, Compositions, Formation mechanism, and neuroprotective effect of compound precipitation from the traditional Chinese prescription huang-Lian-Jie-Du-Tang, Molecules 21 (8) (2016) 1094, https://doi.org/10.3390/molecules21081094.

[7] T. Li, P. Wang, W. Guo, X. Huang, X. Tian, G. Wu, B. Xu, F. Li, C. Yan, X.J. Liang, H. Lei, Natural berberine-based Chinese herb medicine assembled nanostructures with modified antibacterial application, ACS Nano 13 (6) (2019) 6770–6781, https://doi.org/10.1021/acsnano.9b01346.

[8] F. Li, T. Zhe, K. Ma, R. Li, M. Li, Y. Liu, Y. Cao, L. Wang, A naturally derived nanocomposite film with photodynamic antibacterial activity: new prospect for sustainable food packaging, ACS Appl. Mater. Interfaces 13 (44) (2021) 52998–53008, https://doi.org/10.1021/acsami.1c12243.

[9] R. Shi, H. Zhou, Z. Liu, Y. Ma, T. Wang, Y. Liu, C. Wang, Influence of coptis Chinensis on pharmacokinetics of flavonoids after oral administration of radix Scutellariae in rats, Biopharm. Drug Dispos. 30 (7) (2009 Oct) 398–410, https://doi.org/10.1002/bdd.674.

[10] Z. Li, Y. Liu, J. Wang, X. Feng, E.O. Nwafor, Y. Zhang, R. Liu, W. Dang, Q. Zhang, C. Yu, J. Pi, Z. Liu, Baicalin-berberine complex nanocrystals orally promote the co-absorption of two components, Drug Delivery Transl. Res. 12 (12) (2022) 3017–3028, https://doi.org/10.1007/s13346-022-01167-w.

[11] L. Yi, X. Xu, Study on the precipitation reaction between baicalin and berberine by HPLC, J. Chromatogr., B: Anal. Technol. Biomed. Life Sci. 810 (1) (2004) 165–168, https://doi.org/10.1016/j.jchromb.2004.07.007.

[12] H. Wang, T. Li, H. Xiang, X. Zhang, K. Fang, G. Wu, M. Yan, N. Xue, M. Chen, T. Xie, Y. Zhang, P. Wang, H. Lei, Origin and formation mechanism investigation of compound precipitation from the traditional Chinese prescription Huang-Lian-Jie-Du-Tang by isothermal titration calorimetry, Molecules 22 (9) (2017) 1456, https://doi.org/10.3390/molecules22091456.

[13] Mina Wadie, Ezzat M. Abdel-Moety, Mamdouh R. Rezk, Amr M. Mahmoud, Hoda M. Marzouk, Electro-polymerized poly-methyldopa as a novel synthetic mussel-inspired molecularly imprinted polymeric sensor for darifenacin: computational and experimental study, Appl. Mater. Today 29 (2022) 101595, https://doi.org/10.1016/j.apmt.2022.101595.

[14] S.R. LaPlante, N. Aubry, G. Bolger, P. Bonneau, R. Carson, R. Coulombe, C. Sturino, P.L. Beaulieu, Monitoring drug self-aggregation and potential for promiscuity in off-target in vitro pharmacology screens by a practical NMR strategy, J. Med. Chem. 56 (17) (2013) 7073–7083, https://doi.org/10.1021/jm4008714.

[15] S.R. LaPlante, V. Roux, F. Shahout, G. LaPlante, S. Woo, M.M. Denk, S.T. Larda, Y. Ayotte, Probing the free-state solution behavior of drugs and their tendencies to self-aggregate into nano-entities, Nat. Protoc. 16 (11) (2021 Nov) 5250–5273, https://doi.org/10.1038/s41596-021-00612-3.

[16] T. Lu, F. Chen, Multiwfn: a multifunctional wavefunction analyzer, J. Comput. Chem. 33 (5) (2012) 580–592, https://doi.org/10.1002/jcc.22885.

[17] M. Schauperl, P.S. Nerenberg, H. Jang, L.P. Wang, C.I. Bayly, D.L. Mobley, M.K. Gilson, Non-bonded force field model with advanced restrained electrostatic potential charges (RESP2), Commun. Chem. 3 (2020) 44, https://doi.org/10.1038/s42004-020-0291-4.

[18] Humphrey W, Dalke A, Schulten K. VMD: visual molecular dynamics. J. Mol. Graph.. 1996;14(1):33-38, 27-38. https://doi.org/10.1016/0263-7855(96)00018-5..

[19] Lu T, Sobtop, Version 1.0(dev 3.1), http://sobereva.com/soft/Sobtop..

[20] T. Lu, Q. Chen, Independent gradient model based on Hirshfeld partition: a new method for visual study of interactions in chemical systems, J. Comput. Chem. 43 (8) (2022) 539–555, https://doi.org/10.1002/jcc.26812.

[21] D. Van Der Spoel, E. Lindahl, B. Hess, G. Groenhof, A.E. Mark, H.J. Berendsen, GROMACS: fast, flexible, and free, J. Comput. Chem. 26 (16) (2005) 1701–1718, https://doi.org/10.1002/jcc.20291.

[22] F. Neese, Software update: the ORCA program system—version 5.0, Wiley Interdiscip. Rev. Comput. Mol. Sci. (2022), https://doi.org/10.1002/wcms.1606.

[23] T. Lu, Q. Chen, Simple, efficient, and universal energy decomposition analysis method based on dispersion-corrected density functional theory, J. Phys. Chem. A 127 (33) (2023) 7023–7035, https://doi.org/10.1021/acs.jpca.3c04374.

[24] A. González Moreno, P. Prieto, M.C. Ruiz Delgado, E. Domínguez, A. Heredia, A. de Cózar, Structure, isomerization and dimerization processes of naringenin flavonoids, Phys. Chem. Chem. Phys. 23 (33) (2021) 18068–18077, https://doi.org/10.1039/d1cp01161h.

[25] A. Liess, A. Lv, A. Arjona-Esteban, D. Bialas, A.M. Krause, V. Stepanenko, M. Stolte, F. Würthner, Exciton coupling of merocyanine dyes from H- to J-type in the solid state by crystal engineering, Nano Lett. 17 (3) (2017) 1719–1726, https://doi.org/10.1021/acs.nanolett.6b04995.

[26] Z. Wang, J. Lu, Z. Yuan, W. Pi, X. Huang, X. Lin, Y. Zhang, H. Lei, P. Wang, Natural carrier-free binary small molecule self-assembled hydrogel synergize antibacterial effects and promote wound healing by inhibiting virulence factors and alleviating the inflammatory response, Small 19 (2023) e2205528, https://doi.org/10.1002/smll.202205528.

[27] X. Huang, X. Liu, X. Lin, et al., Thermodynamics driving phytochemical self-assembly morphological change and efficacy enhancement originated from single and co-decoction of traditional Chinese medicine, J. Nanobiotechnol. 20 (2022) 527, https://doi.org/10.1186/s12951-022-01734-w.